Characterization and Modeling of Breaking-Induced Spontaneous Nanoscale Periodic Stripes in Metallic Glasses

*Xing Xiang Xia and Wei Hua Wang**

Every day we experience breaks. The rapid fracture of brittle materials such as silica glasses usually releases elastic waves, which in return disturb the local stresses near the crack tip and result in millimeter-scale periodic traces on fracture surfaces, and the spatiotemporal striped patterns have also been observed in a variety of nonequilibrium systems.[1,2] Recently, nanoscale periodic striped patterns have been reported on fracture surfaces of metallic glasses (MGs).[3–10] However, exact characterization of the nanostripes remains lacking and a deep physical understanding of this phenomenon is unclear.[11,12] Here, we systematically investigate the features of the nanoscale periodic patterns in the fracture surfaces of various MGs and attempt to give a comprehensive picture of nanoscale near-tip events and associated energy dissipations in MG breaking. We find that two competing failure mechanisms of immediate meniscus instability and cavitation mechanism near the crack tip control the fracture process of MGs, via detailed observations of the progressive evolution of fine corrugation features along the crack path and the formation process of nanostripes near the crack tip. We propose a model that can capture the main characteristics of the observed nanoscale periodic stripes.

The combination of glassy nature and metallic bonds make the deformation and fracture mechanisms in MGs remarkably different from either crystalline metals or nonmetallic glasses. The plastic deformation of MGs at room temperature is sustained by cooperative shearing of atomic clusters termed shear transformation zones (STZs).[13] The operating of STZs significantly lowers the local viscosity and this unique strain-softening yields a liquid-like zone near the crack tip.[14–16] Therefore, the breaking of MGs has been mimicked by pulling apart a thin viscous layer, like grease, confined between two rigid slides;[14–16] the so-called grease model, involving meniscus instability at the air–grease interface, can explain the formation of typical vein patterns on fracture surfaces. The failure mechanism has been experimentally confirmed by correlating the vein size to the fracture toughness of MGs.[16] However, the fluid meniscus instability at the crack tip cannot predict the nanostripes widely observed for MGs and explain their origin. Further understanding of the nanoscale stripe mechanisms has been limited by the lack of definite experimental observations and characterization since the whole formation process occurs at a nanometer scale. Previous investigations have demonstrated that the universal spontaneously formed nanostripes in MGs have characteristic stripe periods varying approximately from 30 to 120 nm, depending strongly on the specific glassy material.[8,9] Rough estimates show that these nanostripes are quite different from the elastic-wave disturbances because of the ultrahigh frequency of the perturbations (around 10^4 MHz).[3]

Figure 1 A displays the typical fracture surface of prenotched brittle $Mg_{65}Cu_{25}Tb_{10}$ MG rod examined by scanning electron microscopy (SEM) and nanometer-resolution atomic force microscopy (AFM). The fracture surface shows mist and mirror zones, and their transition, along the crack propagation direction (marked by an arrow). High magnification of the mirror zone shows stripes with an average period of approximately 83 nm (see Figure 1B). The straight white lines in Figure 1B, tracing the momentary crack fronts, lie perpendicularly to the crack propagation direction. The uniform spacing indicates the straight crack experiences a steady propagation state and the crack velocity remains nearly constant. The corresponding topography of nanostripes has also been carefully investigated by AFM in tapping mode (see Figure 1C). It is amazing to see that these nanostripes, spontaneously formed during the fracture process of MGs, are almost perfect and the ridges/grooves of the corrugations are smooth even at the nanoscale. The well-defined stripes show an average period of approximately 87 nm, which is consistent with SEM observations. Further cross-sectional analysis in Figure 1C shows that these nanostripes are very shallow; the average depth is roughly 12 nm. AFM examination clearly demonstrated a ridge-to-ridge matching of the nanostripes on complementary surfaces of MGs, which indicate that the nanostripes fundamentally distinguish from the elastic wave markings in silicon glasses.[4]

Numerous experiments have shown that the typical stripe period of brittle MGs has no obvious relation with the loading modes (tension, compression, bending, or impinging)

X. X. Xia, Prof. W. H. Wang
Institute of Physics
Chinese Academy of Sciences
Beijing 100190, PR China
E-Mail: whw@aphy.iphy.ac.cn

DOI: 10.1002/smll.201101785

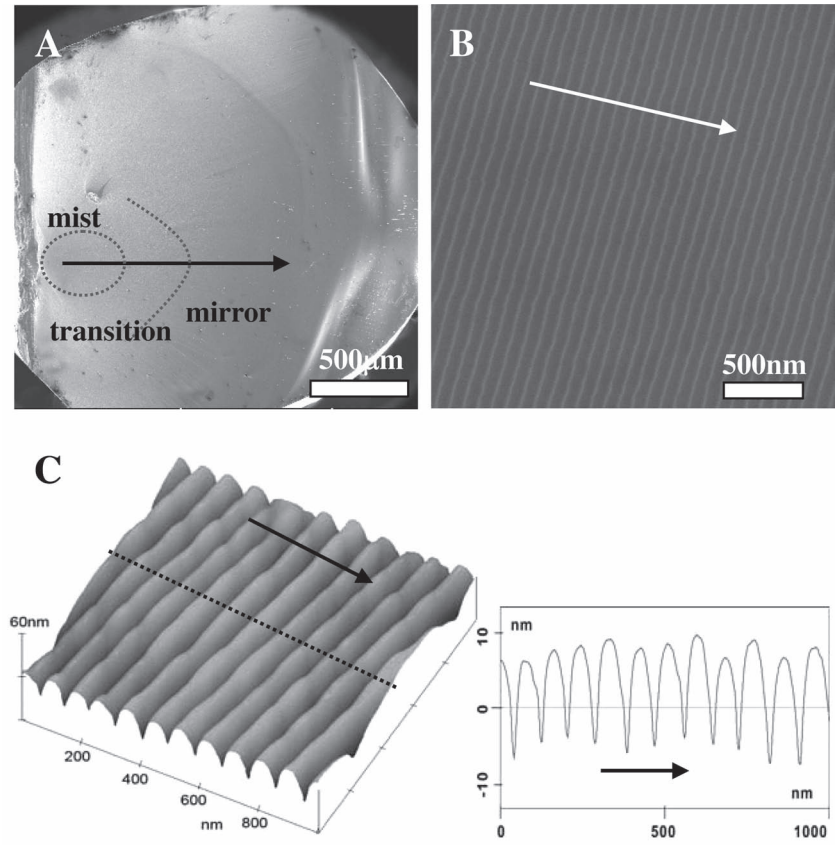

Figure 1. A) A typical fracture surface of Mg-based MG shows distinct mist, transition, and mirror regions along the crack propagation direction (marked by arrow). B) Large-area striped pattern with an average period of approximately 83 nm in the mirror region. C) AFM image displaying the three-dimensional topography of high quality stripes. The average period and depth are about 87 and 12 nm respectively. The spontaneously formed stripes are extremely smooth even at the nanoscale. A colored version of this image is available in the Supporting Information.

or loading rates.[3–9,17–21] For example, during the compression of brittle Mg-based MGs, the sample shatters into many fragments and approximately 83 nm period stripes can be readily found on surfaces of most pieces. In bending tests, the stripe period remains nearly constant (around 83 nm) as the loading rate changes from 0.01 to 10 mm min^{-1}. The characteristic periods of various MGs are summarized in **Figure 2**. One can see that the formation of nanostripes is favored in brittle MGs with low Poisson ratio, such as Mg-, Tb-, and Fe-based MGs, and their period value, ranging approximately from 30 to 120 nm, depends strongly on the specific materials and appears to be a characteristic length in fracture process. The extremely uniform nanostripes over a large area of around 1.0 mm^2, prepared by simply breaking MGs at room temperature, have potential for the development of small devices, such as optical nanogratings.

For brittle MGs, in general, nanoscale dimples and stripes usually dominate the fracture surfaces.[3–5,8] Experimentally, these precursory dimples appear slightly larger than the stripes and it has been speculated that their self-assembly process accounts for the formation of nanostripes.[3,4,9,19] To elucidate the formation mechanism of the nanostripes, high-resolution SEM and AFM have been employed to capture the progressive evolution of morphologies from nanoscale dimples to stripes along the crack path of brittle MGs. **Figure 3** illustrates the gradual transition from approximately 100 nm dense dimples in the mist zone (Figure 1A) to approximately 83 nm periodic stripes in the mirror zone for $Mg_{65}Cu_{25}Tb_{10}$ MG. By slightly tilting the sample in SEM, the wavy shape flank of dimples becomes visible, as shown in Figure 3A1. AFM observations (Figure 3A2) illustrate that each dimple is essentially a hierarchical architecture composed of a fine cavity at the center and four surrounding cones. The segmenting of crack front into periodic cones can be attributed to meniscus instability at the crack tip.[4,5,14–16] Similar smooth cavities are widely observed on tension fracture surfaces of tough MGs and they are considered to be triggered by normal stresses.[22] This coexistence of the periodic cones and cavities indicates apparent dimples stem from the combination of two effects: meniscus instability at the crack tip and cavitations ahead of the crack tip. Actually, some ductile MGs break like crystalline metals via the formation of cavities and subsequent necking.[23] With the crack propagating ahead, as shown in Figure 3B, cones gradually align along the crack front direction to construct ridges with period of around 94 nm in the transition zone. Concomitantly, nanocavities also align and their impressions are evident at the groove bottom. As the crack further proceeds, the alignments of the nanoscale cones and cavities complete and corrugation-shape stripes with a slightly smaller

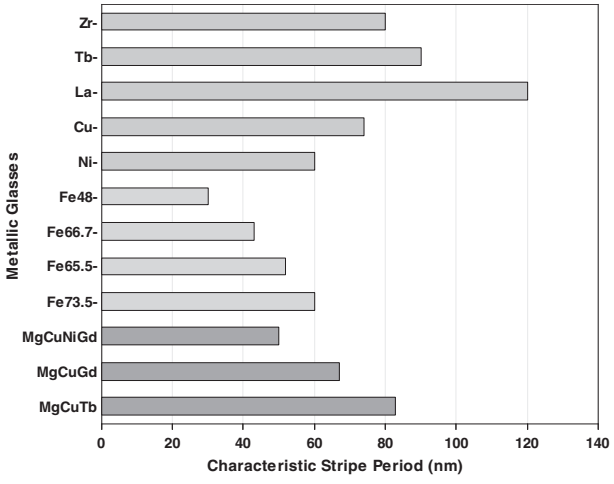

Figure 2. The comparison of the characteristic stripe periods for various MGs. A colored version of this image is available in the Supporting Information.

small NANO MICRO

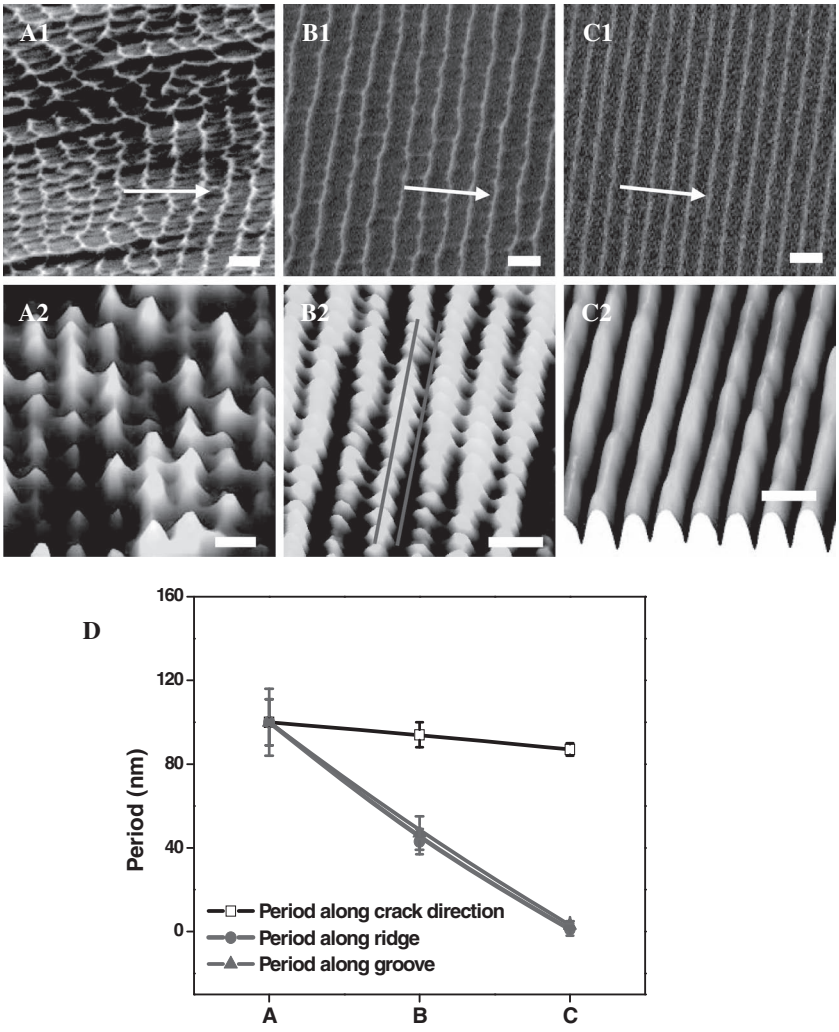

Figure 3. A–C) Progressive evolution of topographical features in mist, mirror, and their transition regions along the crack path (marked by arrows). Scale bars are 100 nm. A1, B1, and C1 are SEM images of dimples, transition and stripes; A2, B2, and C2 are corresponding AFM observations. Images A1 and A2 show apparent dimples in the mist region, which are essentially composed of nanoscale cavities and cones. B1 and B2, in the transition region, show cones or cavities aligned along the crack front direction and the formation of 94 nm period quasi-stripes. C1 and C2 show stripes with a period of 87 nm appearing in the mirror region. D) Quantitative analysis of periods along the crack propagation direction, the ridges, and the grooves. Note the "memory effect" between cavities in grooves and cones along the ridges during the dimple-stripe transition. A colored version of this image is available in the Supporting Information.

period of approximately 87 nm form in the mirror zone (see Figure 3C).

The changes of feature period along both the crack propagation direction and crack front direction during the dimple-to-stripe transition are characterized in Figure 3D. Despite distinct different morphologies, little change has been found between the dimple size (approximately 100 nm) and the final stripe period (approximately 87 nm). The alignment of cones, characterized by the rapid shrinkage of lateral period along the ridges (from 100 nm to 43 nm, and finally to 1 nm), indicates the gradual degeneration of meniscus instability during the transition process. As the stripe formation is completed, the meniscus instability process is nearly negligible and the cavitation process dominates. Most interestingly, the period evolution of cavities in grooves precisely follows that of cones during their alignment processes and this unique "memory effect" implies a directly coupling between two failure mechanisms (see Figure 3B2 and D). We also carefully investigated the formation of nanostripes for Tb-, La-, Zr-, Cu-, and Fe-based MGs and found similar processes.

Based on fracture mechanics and the above observations, we propose a model as illustrated in **Figure 4** to understand the corrugation formation and the fracture process of MGs. We consider a straight, blunted crack. The stress/strain distributions across the liquid-like plastic zone (blue zone) are illustrated in Figure 4A.[24,25] The blunting of the crack tip removes the maximum hydrostatic stress a distance away from the physical crack tip where the strain maximizes, and there exists a high-strain region immediately at the crack tip and a high-stress region within the liquid-like zone. In the high-strain region, as illustrated in Figure 4B, meniscus instability prevails at the air–liquid interface to form a wavy crack front,[14–16] and the breaking of MGs involves the progressive rupture of viscous material by the wavy crack front, producing vein patterns. On the other hand, within the high-stress region, the local stress concentration initiates cavitation (Figure 4B), which is a typical dilatation failure mode of viscous liquid materials.[26] Strikingly, in contrast to the immediate meniscus instability, the cavitation mechanism controls a discontinuous, step-by-step crack advance process. A tunnel-like cavity parallel to the straight blunted crack front spontaneously forms, and a single crack step completes as the cavity links up with the crack. Then, the cavity tip serves as a new crack tip and the whole process repeats itself with a characteristic spacing. As shown in Figure 4C, this unique self-organized cavitation and its repeat process produce nanostripes on fracture surfaces. The experimental observations indeed show the ridge-to-ridge matching nanostripes on opposite surfaces induced by necking of viscous materials between crack tip and cavitations.[4]

Cavitations have been observed during the traction detachment of soft adhesives or viscous liquids highly confined between a substrate and a probe.[26–28] As the probe is pulled away at a high velocity, cavitations preferentially nucleate in the central region of the thin film where the negative hydrostatic pressure is the highest.[26–28] The brittle

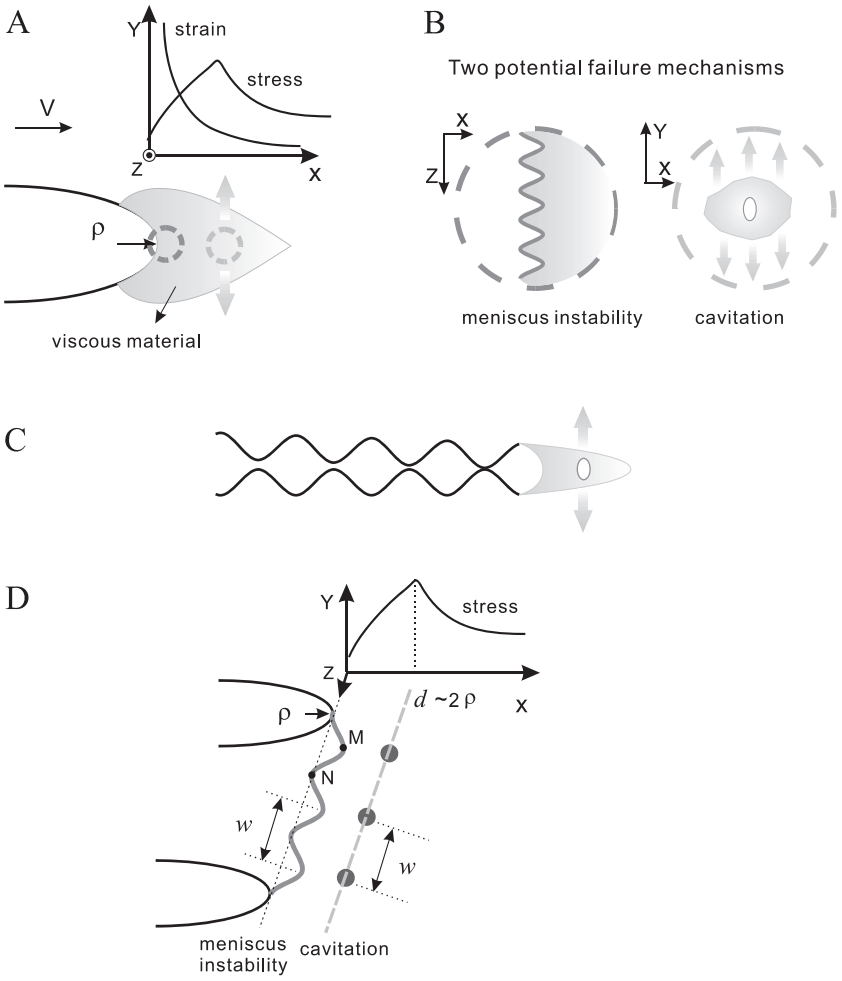

Figure 4. Schematic illustrations of failure mechanisms in MG fracture. A) Viscous liquid-like zone near a blunted crack tip and associated stress or strain distributions. There is a high-strain zone (black dotted circle) immediately at the crack tip, while there is a high-stress zone (grey dashed circle) a distance ahead of the crack tip. B) Two potential failure mechanisms near the crack tip. Meniscus instability prevails at the crack tip and generates a wavy crack front. Cavitation occurs in the high-stress zone. C) Self-organized cavitations ahead of the crack tip and its repeating process. The crack tip experiences a discontinuous, step-by-step advance behavior and produces stripe marking on fracture surfaces. D) Geometric coupling between two mechanisms. Meniscus instability (grey dashed line) causes a lateral periodic stress fluctuation into the high-stress zone and local stress enhancements initiate cavities (filled-in points). Hence, the period of cavities in grooves physically "memorize" the fingering wavelength or cone period. A colored version of this image is available in the Supporting Information.

fracture of MGs essentially involves a tiny liquid-like zone ahead of the blunted crack tip. These viscous mediums are subjected to the concentrated stress near the crack tip and the fracture process can be recognized as a natural probe-tack test. Note that the maximum hydrostatic stress is highly localized within the liquid-like zone where cavitations operate. As cavitations prevail, dimple or stripe patterns appear on fracture surfaces consequently.

The initiation of a cavity ahead of the crack tip is determined by the local hydrostatic stress, which is very sensitive to the crack tip radius, ρ (as shown in Figure 4D).[25] For large ρ the stress concentration is too small to trigger cavitation and only meniscus instability prevails; on te other hand, a small ρ would concentrate a sufficient stress for cavitation. Therefore, there should exist a critical crack tip radius, ρ^*, corresponding to the cavitation initiation within the liquid zone. Due to the complicated rheological properties of the viscous materials, it is difficult to exactly determine a mechanical criterion for the cavitation. To estimate ρ^*, we simplify the complicated cavitation process and focus on the initiation site of cavitation, considering only a simple geometric coupling between two mechanisms. As illustrated in Figure 4D, the cavitation process is regarded as a wavy crack front adding a laterally periodic stress fluctuation into the original high stress region: the concave curvature at point M has increased hydrostatic stress while the convex curvature at point N reduces hydrostatic stress. The periodic stress modulations in the high stress region generate discrete spherical cavitations (not tunnel-like ones) and thus these cavities physically "memorize" the wavy crack front or the period of cones (shown in Figure 3D). The dominant wavelength of the wavy crack front can be described by[15,16]

$$w \approx 2\pi\sqrt{\frac{3\chi}{\mathrm{d}\sigma/\mathrm{d}x}} \tag{1}$$

where χ and $\mathrm{d}\sigma/\mathrm{d}x$ represent the surface tension of viscous materials and the negative pressure gradient in the crack propagation direction, respectively. For rigid-plastic MGs, the $\mathrm{d}\sigma/\mathrm{d}x$ ahead of a blunted crack tip can be roughly expressed as[29]

$$\frac{\mathrm{d}\sigma}{\mathrm{d}x} \approx \frac{\tau_y(1+\pi)}{\rho[\exp(\pi/2)-1]} \tag{2}$$

where τ_y is the shear yield stress ($\tau_y \approx G\gamma_c$, G is shear modulus and γ_c = 0.0267 for MGs[30]). Hence, the lateral wavelength can be simply rewritten as

$$w \approx C\sqrt{\rho} \tag{3}$$

where $C^2 = 12\pi^2\frac{[\exp(\pi/2)-1]\chi}{(1+\pi)G\gamma_c}$. Under the condition that both of the two mechanisms take part in the crack process, this geometric coupling requires that $w \approx d$, where $d \approx 2\rho$ is the location of the high-stress zone from crack tip.[24,25] Then we get the intrinsic lengthscale ρ^* as shown in **Figure 5** for MG breaking,

$$\rho^* \approx \frac{1}{4}C^2 \tag{4}$$

If $\rho > \rho^*$, as illustrated in Figure 5, viscous fingering with the lateral wavelength $w \approx C\rho^{0.5}$ dominates immediately

small NANO MICRO

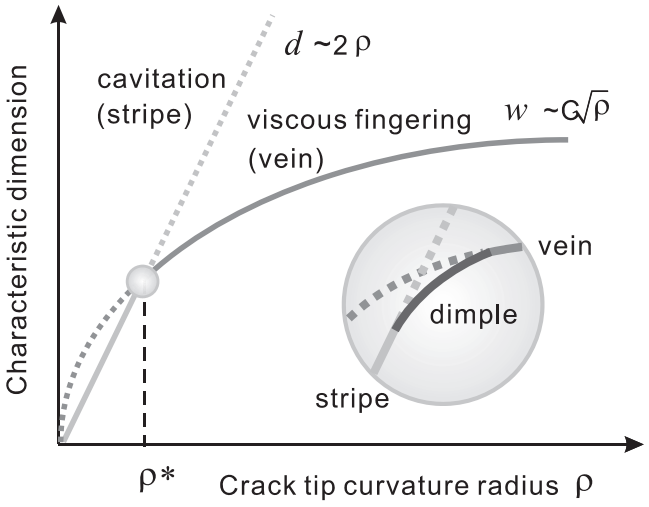

Figure 5. Illustration of the mechanisms involved and a morphology map for the MG breaking process. For a large crack tip radius ρ, viscous fingering with the lateral wavelength $w \approx C\,\rho^{0.5}$ dominates immediately at the crack tip and the failure displays a continuous crack advance manner. Viscous fingering results in typical vein morphology patterns. For small ρ, cavitation is readily generated within the high stress zone (a distance $d \approx 2\,\rho$ ahead of the crack tip) and the self-organized tunnel-like cavitation shows a discontinuous, step-by-step crack advance manner. This cavitation produces rippled fracture surfaces. At the critical crack-tip radius ρ_*, the immediate viscous fingering at crack tip adds a lateral stress fluctuation into the high-stress zone and gives rise to discrete dimples with the period of the fingering wavelength w. Experimentally, the dimples are equiaxial on fracture surfaces and this requires the geometric condition $w \approx d$. The inset shows the evolutions of the vein, dimple, and stripe fracture morphologies with local ρ. A colored version of this image is available in the Supporting Information.

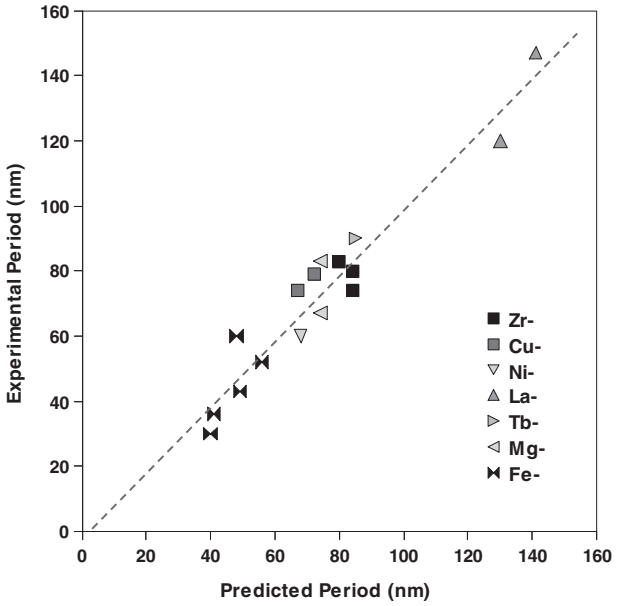

Figure 6. The comparison of our estimated period value of stripes with experimental result for various MGs. Detailed data are listed in Table 1. For most materials, including Zr-, Cu-, Ni-, Mg-, La-, Tb-, and Fe-based MGs, the predictions agree well with experiments. A colored version of this image is available in the Supporting Information.

at the crack tip and the failure displays a continuous crack advance manner. The fracture process is then dominated by immediate meniscus instability at the crack tip and vein patterns appear on fracture surface. If $\rho < \rho*$, the cavitation is readily generated within the high-stress zone (a distance $d \approx 2\rho$ ahead of the crack tip) and the self-organized tunnel-like cavitation shows a discontinuous, step-by-step crack advance manner, and results in regular stripes. When $\rho \approx \rho*$, the cooperation of the two mechanisms leads to the formation of dimple-like structures.

The crack tip radius becomes small as the crack accelerates into the liquid zone. As the actual curvature radius approaches $\rho*$, discrete cavitations or dimple cores are initially triggered within the high-stress zone. The characteristic stripe period can be roughly estimated as the distance of this high stress zone ahead of the crack tip:

$$d \approx 2\rho* \approx 6\pi^2 \frac{\exp(\pi/2) - 1}{(1+\pi)\gamma_c} \frac{\chi}{G} \approx 2040 \frac{\chi}{G} \qquad (5)$$

From Equation 5 one can see that the formation and the characteristic stripe period are mainly determined by two factors: the surface tension of the viscous liquid and the shear modulus of the MG. This can be easily understood since the fracture process involves breaking of viscous liquid embedded in an elastic body. For MGs, the typical values of χ and G are on the order of 1 N m^{-1}[31,32] and 10 to 90 GPa,[30] respectively. The stripe period of various MGs is then predicted to be 20 to 200 nm, which is consistent with the experimental results of 30 to 150 nm. **Figure 6** shows the comparison between the estimated period from our model and the experimental period of stripes for various MGs. The data are listed in **Table 1**, and we estimated χ of glass-forming liquids by following proportional addition of pure components.[32] The stripe periods and features for Zr-, Cu-, Ni-, Mg-, Tb-, La-, and Fe-based MGs agree well with the theoretical predictions.

Our model proposes an intrinsic lengthscale $\rho*$, determined only by χ and G, in the MG breaking process, which controls the localized fracture events. At large crack tip radius ρ ($\rho > \rho*$), the fracture is a simply continuous and progressive crack growth process, while for small ρ ($\rho \leq \rho*$), self-organized cavitations occur, the crack tip experiences a discontinuous, step-by-step advance process, and the quantized growth steps result in stripe markings on the fracture surfaces of the MG. The critical value of $\rho*$ for MGs is typically about 10 to 100 nm, the stripes (expected to be around $2\rho*$) appear more easily for brittle MGs. The proposed cavitation-induced rippled morphology has also been simulated during fracturing of elastic–plastic materials.[35] The good agreement between prediction and experimental observations indicates that, in spite of its simplicity, our model captures and simulates the characteristics of the observed periodic stripes in MGs for the first time; thus, the model might provide useful insight into the fracture process and associated fracture surface roughening of MGs. Additionally, according to the model, the period of characteristic stripes can be tailored by tuning χ and G,

Table 1. Characteristic stripes for various metallic glasses. The surface tensions of glass-forming liquids are measured at their liquidus temperatures or calculated based on the simple rule of mixtures.[31,32] The shear modulus is obtained by using an ultrasonic method.

MG composition [at-%]	Surface tension χ [N m^{-1}]	Shear modulus G [GPa]	d^{Calc} [nm]	d^{Expt} [nm]	Sample	Loading mode	Reference
$Zr_{41.2}Ti_{13.8}Cu_{10}Ni_{12.5}Be_{22.5}$	1.47[a)]	35.9	84	80	Plate	High velocity impact	[8]
$Zr_{55}Al_{22.5}Co_{22.5}$	1.47[a)]	37.6	80	83	Ribbon	Tension	This work
$(Zr_{50.7}Cu_{28}Ni_9Al_{12.3})_{99}Gd_1$	~1.4	34.0	84	74	Rod	Compression	[33]
$Cu_{46}Zr_{42}Al_7Y_5$	1.09[a)]	31.0	72	79	Rod	Bending	This work
$Cu_{49}Hf_{42}Al_9$	~1.4	42.7	67	74	Rod	Compression	[18]
$Ni_{42}Cu_5Ti_{20}Zr_{21.5}Al_8Si_{3.5}$	~1.6	47.5	68	60	Rod	Compression	[6]
$La_{55}Al_{25}Ni_{10}Cu_5Co_5$	~1.0	15.6	130	120	Rod	Compression	[17]
$La_{62}Al_{14}Cu_{11.7}Ag_{2.3}Ni_5Co_5$	~0.9	13.0	141	147	Rod	Bending	This work
$Tb_{36}Y_{20}Al_{24}Co_{20}$	~1.0	24.0	85	90	Rod	Bending	This work
$Mg_{65}Cu_{25}Tb_{10}$	~0.7	19.3	74	83	Rod	Bending	This work
$Mg_{65}Cu_{25}Gd_{10}$	~0.7	19.3	74	67	Rod	Bending	[4]
$Mg_{65}Cu_{20}Ni_5Gd_{10}$	~0.7	–	–	50	Rod	Bending	[5]
$Fe_{73.5}Cu_1Nb_3Si_{13.5}B_9$	~1.6[b)]	68[c)]	48	60	Ribbon	Tension	[19]
$Fe_{65.5}Cr_4Mo_4Ga_4P_{12}C_5B_{5.5}$	~1.6[b)]	58.5	56	52	Rod	Compression	[7]
$Fe_{66.7}Cr_{2.3}Mo_{4.5}P_{8.7}C_7B_{5.5}Si_{3.3}Al_2$	~1.6[b)]	66.8	49	43	Rod	Compression	[21]
$Fe_{48}Cr_{15}Mo_{14}Er_2C_{15}B_6$	~1.6[b)]	81.0	40	30	Rod	Compression	[20]
$Fe_{56}Mn_5Cr_7Mo_{12}Er_2C_{12}B_6$	~1.6[b)]	80	41	36	Rod	Bending	This work

[a)]Experimentally determined using the drop oscillation technique with a n accuracy of ±5%;[31] [b)]Experimentally determined using the maximum bubble pressure method;[34] [c)]Estimated using the uniaxial yield strength of 3.3 GPa and the universal shear elastic limit of 0.026.

which is useful for application design. We note that the discontinuous crack advance process is abundant in nature, and spatiotemporal striped patterns have also been observed in a variety of nonequilibrium systems in nature, including vertically vibrated granular layers, Rayleigh-Benard convection cells, and ferromagnetic films with dipolar interactions.[1,2] Similarities between our observed striped pattern and the spatiotemporal striped patterns in these nonequilibrium systems are found.[9] The characterization and modeling of the nano-scale striped patterns in fracture surface of metallic glasses may have implications for understanding the origin of this kind of nonequilibrium phenomenon.

Experimental Section

The Mg-, Tb-, Fe-, Cu-, and La-based bulk MGs were prepared by arc melting with pure metal elements in a Ti-gettered argon atmosphere. The ingots were remelted and suck-cast into a Cu mould under an argon atmosphere to get a cylindrical rod of 3 mm diameter. The $Zr_{55}Al_{22.5}Co_{22.5}$ glassy ribbon was produced via melt spinning. The amorphous nature of the as-cast alloys was ascertained by x-ray diffraction (XRD). These materials were selected for our experiments because they are brittle and stripes are easily formed.

The samples for three-point bending test with lengths of 30 mm were cut from the rod samples by means of electrical discharge machining. A seed notch with depth of 0.5 mm was introduced by a diamond saw in the center of the specimen. Three-point bending and tension tests were performed on an Instron machine and the crosshead moving velocities were chosen as 0.01, 0.1, 1, and 10 mm min^{-1}. The experiments were repeated at least five times to confirm the experiment results. The fresh fracture surfaces were examined using a Philips XL30 environmental instrument for scanning electron microscopy (SEM) and a Digital Instruments NanoScope IIIa D-3000 for atomic force microscopy (AFM). No obvious crystallization was observed in the fracture surface by XRD and TEM. The conducting MGs make the fracture surfaces be conveniently investigated on a nanometer scale by HRSEM and AFM, synchronously providing more information about the crack propagation at higher spatial resolution and giving a three-dimensional view. The elastic parameters, i.e., elastic modulus, shear and longitudinal wave speeds, and Poisson ratio of the samples were measured using an ultrasonic method.

Supporting Information

Supporting Information is available from the Wiley Online Library or from the author.

Acknowledgements

Discussions and experimental assistance from X. K. Xi, D. Q. Zhao, D. W. Ding, and H. Y. Bai are appreciated. Financial support is acknowledged from the NSF of China (nos. 50731008 and 50921091) and MOST 973 of China (nos. 2007CB613904 and 2010CB731603). W.H.W. designed the research. X.X.X. carried out the experiments. X.X.X. and W.H.W. analyzed the results and wrote the paper. The authors declare no competing financial interests.

[1] I. S. Aranson, L. S. Tsimring, *Rev. Mod. Phys.* **2006**, *78*, 641–692.
[2] M. C. Cross, P. C. Hohenberg, *Rev. Mod. Phys.* **1993**, *65*, 851–1112.
[3] X. K. Xi, D. Q. Zhao, M. X. Pan, W. H. Wang, Y. Wu, J. J. Lewandowski, *Appl. Phys. Lett.* **2006**, *89*, 181911.
[4] G. Wang, D. Q. Zhao, H. Y. Bai, M. X. Pan, A. L. Xia, B. S. Han, X. K. Xi, Y. Wu, W. H. Wang, *Phys. Rev. Lett.* **2007**, *98*, 235501.
[5] D. G. Pan, H. F. Zhang, A. M. Wang, Z. G. Wang, Z. Q. Hu, *J. Alloys Compd.* **2007**, *438*, 145–149.
[6] J. Shen, W. Z. Liang, J. F. Sun, *Appl. Phys. Lett.* **2006**, *89*, 121908.
[7] Z. F. Zhang, F. F. Wu, W. Gao, J. Tan, Z. G. Wang, M. Stoica, J. Das, J. Eckert, B. L. Shen, A. Inoue, *Appl. Phys. Lett.* **2006**, *89*, 251917.
[8] M. Q. Jiang, Z. Ling, J. X. Meng, L. H. Dai, *Philos. Mag.* **2008**, *88*, 407–426.
[9] Y. T. Wang, X. K. Xi, G. Wang, X. X. Xia, W. H. Wang, *J. Appl. Phys.* **2009**, *106*, 113528.
[10] Y. Braiman, T. Egami, *Physica A* **2009**, *388*, 1978–1984.
[11] B. N. Cox, H. Gao, D. Gross, D. Rittel, *J. Mech. Phys. Solids* **2005**, *53*, 565–596.
[12] J. Fineberg, M. Marder, *Phys. Rep.* **1999**, *313*, 1–108.
[13] A. S. Argon, *Acta Metall.* **1979**, *27*, 47–58.
[14] C. A. Pampillo, *J. Mater. Sci.* **1975**, *10*, 1194–1227.
[15] F. Spaepen, *Acta Metall.* **1975**, *23*, 615–620.
[16] A. S. Argon, M. Salama, *Mater. Sci. Eng.* **1976**, *23*, 219–230.
[17] N. Nagendra, U. Ramamurty, T. T. Goh, Y. Li, *Acta Mater.* **2000**, *48*, 2603–2615.
[18] S. V. Madge, T. Wada, D. V. Louzguine-Luzgin, A. L. Greer, A. Inoue, *Scr. Mater.* **2009**, *61*, 540–543.
[19] G. Wang, Y. T. Wang, Y. H. Liu, M. X. Pan, D. Q. Zhao, W. H. Wang, *Appl. Phys. Lett.* **2006**, *89*, 121909.
[20] R. D. Ma, H. F. Zhang, H. S. Yu, Z. Q. Hu, *J. Alloys Compd.* **2008**, *454*, 370–373.
[21] H. X. Li, K. B. Kim, S. Yi, *Scr. Mater.* **2007**, *56*, 1035–1038.
[22] Z. F. Zhang, J. Eckert, L. Schultz, *Acta Mater.* **2003**, *51*, 1167–1179.
[23] E. Bouchaud, D. Boivin, J. L. Pouchou, D. Bonamy, B. Poon, G. Ravichandran, *Europhys. Lett.* **2008**, *83*, 66006.
[24] R. K. Nalla, J. H. Kinney, R. O. Ritchie, *Nat. Mater.* **2003**, *2*, 164–168.
[25] *Fundamentals of Fracture Mechanics* (Ed: J. F. Knott), Butterworth, London **1973**.
[26] S. Poivet, F. Nallet, C. Gay, P. Fabre, *Europhys. Lett.* **2003**, *62*, 244.
[27] C. Gay, L. Leibler, *Phys. Today* **1999**, *52*, 48–52.
[28] H. B. Zeng, B. X. Zhao, J. N. Israelachvili, M. Tirrell, *Macromolecules* **2010**, *43*, 538–542.
[29] *Physics of Strength and Plasticity* (Ed: A. S. Argon) MIT Press, Cambridge, London **1969**.
[30] W. L. Johnson, K. Samwer, *Phys. Rev. Lett.* **2005**, *95*, 195501.
[31] S. Mukherjee, W. L. Johnson, W. K. Rhim, *Appl. Phys. Lett.* **2005**, *86*, 014104.
[32] *The Physical Properties of Liquid Metals* (Eds: T. Iida, R. I. L. Guthrie), Clarendon, Oxford **1988**.
[33] Y. J. Sun, X. S. Wei, Y. J. Hang, J. Shen, *Acta Metall. Sinica* **2009**, *45*, 243–248.
[34] H. H. Liebermann, *J. Mater. Sci.* **1987**, *19*, 1391–1396.
[35] A. P. Kfouri, *Eng. Fract. Mech.* **2008**, *75*1815–1828.

Received: August 31, 2011
Published online: February 15, 2012

